



Engineering pore-size distribution of metal-loaded carbon catalysts by in situ cavitation for boosting electrochemical mass transfer[☆]

Hong-Gang Du ^{a,1}, Xue-Feng Zhang ^{a,1}, Li-Wen Ding ^a, Juan-Li Liu ^{c,*}, Li-Hong Yu ^a, Xiao-Han Zhang ^a, Yuhai Dou ^{b,*}, Li-Ming Cao ^a, Jia Zhang ^a, Chun-Ting He ^a

^a Key Lab of Fluorine and Silicon for Energy Materials and Chemistry of Ministry of Education, College of Chemistry and Chemical Engineering, Jiangxi Normal University, Nanchang 330022, China

^b Institute of Energy Materials Science, University of Shanghai for Science and Technology, Shanghai 200093, China

^c Analytical and Testing Center, Chongqing University, Chongqing 400030, China



ARTICLE INFO

Keywords:

Oxygen evolution reaction
Carbon support
Pore structure
Metal-organic framework
Mass transfer

ABSTRACT

In addition to highly active catalytic sites, mass transfer, especially diffusion of the reactant/product also play important roles in supported electrocatalyst systems. However, compared with the morphologies and specific surface areas, the pore structures of the catalyst supports and their influence on catalytic mass transfer have received less attention. Herein, we propose a universal *in situ* cavitation strategy to regulate the pore size distributions on the metal-loaded carbon through nitro modification on the molecule-based precursors, without significantly changing the electronic structures of the active metal centers. Gas sorption experiments, electrocatalytic measurements and molecular dynamic simulations certified that the increasing mesopore/macropore ratios can remarkably facilitate the diffusion coefficient, enabling improved oxygen evolution kinetics with 71 mV overpotential dropping at 10 mA·cm⁻² compared with the nitro-free counterpart. This work demonstrates that the pore size distributions of the catalyst support should be another nonnegligible parameter on boosting the overall electrocatalytic performance.

1. Introduction

Water electrolysis powered by renewable electricity is an important technology to obtain green hydrogen for promoting global carbon neutrality. However, it is hindered by the key half-reaction called oxygen evolution reaction (OER), which needs highly active, assured persistent, and inexpensive electrocatalysts to bypass multi-step energy barrier for continuously accelerating the kinetics of water splitting [1]. For the design of satisfactory electrocatalysts, not only active sites, but also the electron transport [2,3] and mass transfer [4,5] must be considered. Supported electrocatalysts (SECs) could be potentially candidates, as it is a very effective way to integrate dispersed metal sites and connective electron/substrate transport channels by loading metal-based nanoparticles (MNPs) on conductive supports, such as porous carbons [6,7]. On the one hand, the supported MNPs are uniformly distributed with accessible active sites with multi-component synergy. On the other hand, the supports can not only serve as

confinement protector to avoid agglomeration and degradation of MNPs under working conditions, but also provide significant metal-support interaction to optimize the electronic structures of metal centers [8,9]. To date, lots of successful cases have been achieved on the control of the geometries [10,11], coordination environments [12,13], and electronic structures [14,15] of MNPs on SECs. On the contrary, the influences of the support materials and their pore structures on the electrocatalytic performances, especially the mass transfer, have received little attention [16,17]. Generally, pores in solid materials can be divided into three categories based on their sizes: less than or equal to 2.0 nm for micropores, 2.0–50 nm for mesoporous pores, and greater than or equal to 50 nm for large pores. The dominant contribution to the commonly used Brunauer-Emmett-Teller (BET) specific surface area, determined through gas adsorption measurements, typically originates from micropores, that is, increasing the proportion of micropores can enhance the BET specific surface area. Therefore, in theory, a higher proportion of micropores is beneficial for improving the contact surface area

[☆] Optional Dedication.

^{*} Corresponding authors.

E-mail addresses: liujuanli_19@cqu.edu.cn (J.-L. Liu), y.dou@usst.edu.cn (Y. Dou), hct@jxnu.edu.cn (C.-T. He).

¹ These authors contributed equally.

between the catalyst and the electrolyte/substrate, thereby enhancing the effective electrochemical specific surface area. Currently, there are many reports on SECs that have relate the catalytic performance to the geometric area of the pore surface, such as BET specific areas, but exact factors that actually affect the mass transfer, eg. pore size and/or pore distributions, remain poorly understood [18,19]. Actually, in catalytic processes, the diffusion behavior of substrate and product molecules within the pores and their interactions with the pore walls are another important factor that must be considered. Different pore sizes or pore distributions can have varying effects on mass transfer due to confinement effects, yet it is often overlooked during molecule design of catalysts.

To study the structure-property relationship in this context, it is first necessary to find effective methods for controlling the pore structures of catalyst supports. As the most common SECs, metal-carbon composites have shown great potential in energy-related electrocatalysis due to their abundant pores, yet the precise regulation of carbon pore structures still remains a challenge since the amorphous nature of this support [20]. In recent years, the use of well-defined metal-organic frameworks (MOFs) as precursors have provided a very effective platform for designing novel metal-carbon composite materials with high porosity, conductivity as well as remarkable catalytic performances [21–25]. Due to the space confinement of nano-pores and/or the coordination confinement of organic ligands, MOFs as precursors have natural advantages for reducing the migration and aggregation of metal species during synthesis and electrocatalysis, being beneficial for the preparation of ultrafine MNPs [26–28]. These MNPs often contain multiple metal species which can promote the catalytic activity through synergistic effect between different kind of metal atoms. Furthermore, their highly tunable organic ligands provide new opportunities for the regulation on the derived carbon matrix, such as microtopography [29], heteroatom doping [30], elemental ratio [31], defects [32] and so on. Actually, rational modification of the organic building blocks and/or network topology could also enable directional tuning the pore structures of the derived carbon supports, which is conducive to the disclosure of their structure-activity relationship on electrocatalysis.

Herein, a universal *in situ* cavitation strategy is developed to modulate the pore size distributions on the carbon support of metal-carbon composites through introducing nitro group into the MOF precursors. For the first time, we specifically investigated the effect of different scale nanopores on the catalytic mass transfer and electrocatalytic performance. The increasing mesopore/macropore proportion endowed the as-synthesized FeNi alloy loaded porous carbon catalyst (FeNi@PC) with significantly enhanced OER activity.

2. Experimental section

2.1. Materials

Unless otherwise specified, the involved chemicals were purchased from Aladdin (China, Shanghai) and all of them are analytical grade. The detailed purity is as follows: Nickel nitrate hexahydrate (99.0%), zinc nitrate hexahydrate (99.0%), 5-nitroisophthalic acid (98.0%), isophthalic acid (99.0%), 4,4'-bipyridine (98.0%), N,N-dimethylformamide (99.5%), KOH (semiconductor grade, 99.9%), iron nitrate nonahydrate (98.5%). All the experiments were adopted ultrapure water, meeting the following specifications: resistivity of at least $18 \text{ M}\Omega\cdot\text{cm}^{-1}$, conductivity not exceeding $0.1 \mu\text{s}\cdot\text{cm}^{-1}$, and TOC levels below 10 ppb. The ultrapure water was obtained from a laboratory-installed Milli-Q ultrapure water system.

2.2. Sample preparation

Synthesis of trimetallic MOF precursors ZnFeNi-MOF-R ($R = \text{NO}_2, \text{H}$): The synthesis method was improved from the previous works [33]. Taking ZnFeNi-MOF- NO_2 with Zn: Fe: Ni = 20: 1: 1 (molar ratio) as an

example. Typically, $\text{Zn}(\text{NO}_3)_2\cdot 6\text{H}_2\text{O}$ (1.141 g, 3.836 mmol), 2.91 mL $\text{Fe}(\text{NO}_3)_3\cdot 9\text{H}_2\text{O}$ aqueous solution (0.066 M) and, 5-nitroisophthalic acid (0.880 g, 4.22 mmol), 4,4'-bipyridine (0.659 g, 4.22 mmol) and 2.91 mL $\text{Ni}(\text{NO}_3)_2\cdot 6\text{H}_2\text{O}$ aqueous solution (0.066 M) were dissolved in DMF (44.18 mL). Subsequently, under a continuous flow of N_2 gas, the mixed solution was stirred for 24 h at 120 °C. The obtained solution was cooled to room temperature, and the precipitate was stirred for 4 h in fresh methanol and filtrated. Finally, to obtain ZnFeNi-MOF- NO_2 , the powder was subjected to drying at 60 °C under vacuum for 24 h (1.71 g, Yield: 94.3%, based on Zn). ZnFeNi-MOF- NO_2 with other metal ratios (Zn: Fe: Ni = 10: 1: 1, 15: 1: 1, 25: 1: 1 and 30: 1: 1) were obtained by changing the metal feeding. For comparison, the nitro-free precursors of ZnFeNi-MOF-H with the same metal ratios were also synthesized with similar procedures by just changing the ligand of 5-nitroisophthalic acid to isophthalic acid. The synthesis steps of ZnM-MOF- NO_2 ($M = \text{Fe}, \text{Ni}$) are identical to that of ZnFeNi-MOF- NO_2 , except that $\text{Ni}(\text{NO}_3)_2\cdot 6\text{H}_2\text{O}$ or $\text{Fe}(\text{NO}_3)_3\cdot 9\text{H}_2\text{O}$ is not added during the feeding process. The yield of ZnFe-MOF- NO_2 is 96.4%, and the yield of ZnNi-MOF- NO_2 is 82.7%, based on Zn.

Synthesis of NiFe_2O_4 : first, we synthesized NiFeOOH following the research of Feng Rong et al. [34], and then pyrolyzed it under a nitrogen atmosphere to obtain NiFe_2O_4 . Typically, 8.8 mL of tetramethylammonium hydroxide (TMAOH) solution, 4 mL of hydrogen peroxide (30 wt %), and 27.2 mL of water were mixed together to obtain a 40 mL aqueous solution. Add the above-mentioned solution to a flask containing 20 mL of $\text{NiCl}_2\cdot 6\text{H}_2\text{O}$ and $\text{FeCl}_3\cdot 6\text{H}_2\text{O}$ (0.3 M, with a Ni/Fe molar ratio of 1). The obtained suspension was vigorously stirred at 30 °C for 24 h. The precipitate was separated by filtration, washed with a large amount of deionized water and eth-anol, dried overnight at 60 °C, resulting in NiFeOOH . NiFeOOH was pyrolyzed at 500 °C under an N_2 atmosphere for two hours to obtain the NiFe_2O_4 (yield: 54%).

Synthesis of porous carbon supported FeNi nanoalloy FeNi@PC-R ($R = \text{NO}_2, \text{H}$): The composite catalysts were derived by subjecting the MOF precursors to a pyrolysis process at 1000 °C under N_2 atmosphere for 30 min, with a heating rate of $10 \text{ }^{\circ}\text{C}\cdot\text{min}^{-1}$, and the products were denoted as FeNi@PC- NO_2 (Yield: 13.0%). For comparison, FeNi@PC-H, FeNi@PC- NO_2 with other metal ratios (Zn: Fe: Ni = 10: 1: 1, 15: 1: 1, 25: 1: 1 and 30: 1: 1), Fe@PC- NO_2 and Ni@PC- NO_2 were also synthesized with similar procedures by just changing the ligands or the metal contents.

2.3. Characterization

Powder X-ray diffraction (PXRD) patterns were obtained using a Miniflex600 diffractometer, with a wavelength of 0.154 nm for $\text{Cu-K}\alpha$ radiation. Field emission electron microscopy (FESEM) images were obtained on Hitachi SU8010 high resolution field emission scanning electron microscopy. Scanning electron microscopy (SEM) images were acquired using a ZEISS EVO 10 scanning electron microscope, with an operating accelerating voltage of 30 kV. High-resolution transmission electron microscopy (HRTEM) was conducted using a FEI Tecnai G2 F30 TEM. Inductively Coupled Plasma Optical Emission Spectroscopy (ICP-OES) was used with the Agilent 730 instrument to analyze the elemental content. Nitrogen sorption isotherms of the samples were collected on a Micrometrics ASAP2020 Plus instrument at 77 K, and the pore size distributions were obtained from the adsorption segments by using different methods of 2D-NLDFT- $\text{N}_2\text{-CFP-4}$ (CFP-4), 2D-NLDFT- $\text{N}_2\text{-CFP-6}$ (CFP-6), DFT Model, CFP-AS4-2D-NLDFT (CFP-AS4), CFP-AS6-2D-NLDFT (CFP-AS6), CFP-AS12-2D-NLDFT (CFP-AS12), CSP-NLDFT and NLDFT-SD3- $\text{N}_2\text{-77-CSP}$ (NLDFT-SD3). Before sorption experiments, the sample, weighing approximately 120 mg, was loaded into the sample a quartzs tube and heated in high vacuum conditions at 150 °C to eliminate any remaining guest molecules. Fourier Transform Infrared (FT-IR) spectroscopy was performed using the Nicolet 6700 FTIR instrument. Raman spectrometer (LabRAM HR, Horiba Jobin Yvon, France) was utilized to capture Raman spectra within the 800–2000 cm^{-1} spectral

range. The thermal stability of samples was analyzed by TGA 55 thermogravimetric analyzer in a nitrogen atmosphere ranging from room temperature to 800 °C. Thermo ESCALAB 250Xi spectrometer with an Al K X-ray source energy of 1486.6 eV was utilized for X-ray photoelectron spectroscopy (XPS), and the energy scale of the instrument was calibrated using C1s (284.8 eV). The contact angle was measured by Dataphysics OCA20 at room temperature. The gas product was analyzed by gas chromatography (GC-7820) with a thermal conductivity detector.

2.4. Electrochemical measurements

Electrochemical measurements were conducted at room temperature using a conventional three-electrode electrochemical cell on a CHI 760 electrochemical workstation (Shanghai Chenhua, China). A glassy carbon electrode with a diameter of 5 mm was used as the working electrode, and a Hg/HgO electrode was used as the reference electrode, while a platinum plate was served as the counter electrode. The as-prepared electrocatalysts (2 mg) were dispersed in mixed solutions of 25 μL Nafion177 solution (~5% in a mixture of lower aliphatic alcohols and water), 150 μL water and 150 μL isopropanol, and then ultrasonic treatment for 60 min to obtain uniform inks. Subsequently, 10 μL of the ink was dropped onto a clean GCE to form a catalyst film. When using carbon cloth (1 cm × 1 cm) as the working electrode, the prepared electrocatalyst (5.0 mg) was dispersed in a mixture of 25 μL Nafion 177 solution, 150 μL water, and 150 μL isopropanol. The mixture was then sonicated to obtain a uniform ink. Subsequently, 40 μL of the ink was dropped onto nitric acid-treated carbon cloth to form the catalyst film. The electrolyte was subjected to continuous N₂ bubbling for 50 min before the measurements to eliminate dissolved O₂. Linear sweep voltammetry (LSV) tests were conducted at a scan rate of 5.0 mV•s⁻¹ with and without 98% *iR* compensation (Fig. S14). The measurement range of the electrochemical impedance spectroscopy (EIS) was from 10⁵ to 10⁻² Hz, with an AC amplitude of 5 mV. Measurement of the long-term stability was performed using the chronoamperometry method. The Faraday efficiency of the catalyst was defined as the ratio of experimentally measured O₂ to theoretically calculated O₂. The electrochemically active surface area (ECSA) and roughness factor (R_f) of catalysts are evaluated using the following equations:

$$\text{ECSA} = C_{\text{dl}} / C_s \quad (1)$$

$$R_f = \text{ECSA} / A_g \quad (2)$$

In the non-Faradaic region, the double-layer capacitance of C_{dl} was derived from the double-layer charging curves of the catalysts at various scanning rates by cyclic voltammetry (CV) scans. C_s represents the standard capacitance per unit area of the atomically flat surface of the respective materials under the same experimental conditions, and herein we adopted $C_s = 0.040 \text{ mF} \cdot \text{cm}^{-2}$ based on previous works [35–37]. R_f was determined by dividing the ECSA by 0.196 cm², which corresponds to the geometric area of the electrode (A_g). The *i-t* transient curves were measured between 1 ms and 10 s (if the potential step experiment time is too short, it will be controlled by the charging current, and if the experiment time is too long, it will be interfered by natural convection) at a constant temperature and static solution. To exclude the influence of gas bubbles, for each *i-t* transient test, the electrode was taken out and static for two minutes before the next test. A straight line through the origin can be obtained by taking $t^{-1/2}$ as the *x*-axis and *j* as the *y*-axis. Then, the diffusion coefficient is calculated according to the slope of the line and the Cottrell equation. In the hermetically-sealed H-type electrochemical cell, the measurement of Faradaic efficiency was conducted. The generated gas was qualitatively analyzed using gas chromatography (GC-7820 equipped with a thermal conductivity detector). The actual oxygen production is calculated using the ideal gas state equation $PV=nRT$, where P represents the atmospheric pressure; V is the volume of the gas above the electrolyte solution; R is the ideal gas constant; T is the room temperature; and n is the

actual amount of oxygen produced within a certain period of time. The theoretical oxygen production is calculated using Faraday's law equation $Q=nzF$, where Q represents the amount of charge required for electrolysis in a certain period of time, which can be calculated based on the current I and time t during the electrolysis process; n is the theoretical calculated oxygen production; z is the number of electrons transferred in the electrochemical reaction; and F is Faraday's constant. Faradaic efficiency is the ratio between the actual oxygen production and the theoretical one.

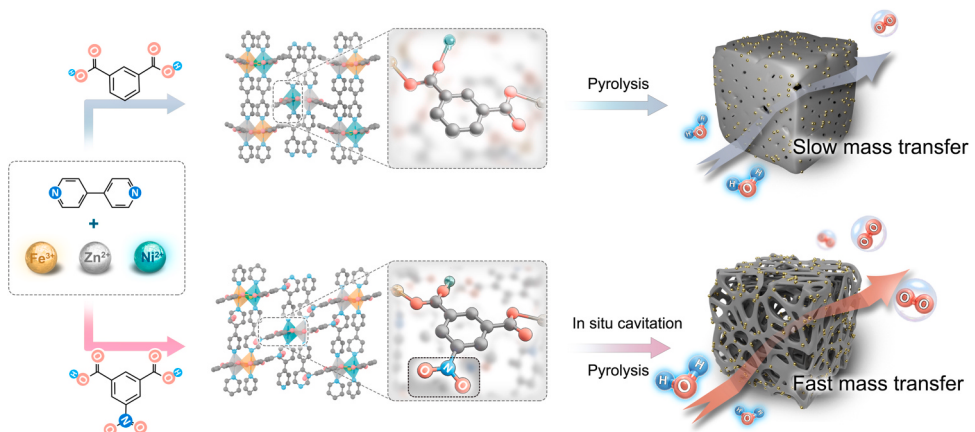
2.5. Theoretical methods

The Cambridge Sequential Total Energy Package (CASTEP) module in the Materials Studio software was used for the DFT calculations involving geometric optimization, energy relaxations, and electron density differences. The spin-polarized DFT with plane wave pseudo-potential methods were adopted. The exchange-correlation functional in the generalized gradient approximation (GGA) was described by the Perdew-Burke-Ernzerhof (PBE) functional, along with the use of OTFG ultrasoft pseudopotentials, Koelling-Harmon relativistic treatment in the calculations. The plane wave energy cutoff was set to 450 eV, and the convergence criteria for stresses, forces, energy and displacements were set at $5 \times 10^{-2} \text{ GPa}$, $3 \times 10^{-2} \text{ eV} \cdot \text{\AA}^{-1}$, $1 \times 10^{-5} \text{ eV} \cdot \text{atom}^{-1}$ and $1 \times 10^{-3} \text{ \AA}$, respectively. Molecular dynamic simulations were performed in periodic boxes containing 112 H₂O molecules for 10 Å pore model and 336 H₂O molecules for 30 Å pore model. During the structure optimizations and MD processes, all carbon atoms of the two graphene layers were fixed. The partial atomic charges of atoms were calculated using the charge equilibration (QE) method. The constant-volume & temperature (NVT) ensemble and Dreiding forcefield were implemented in the MD simulations and Random initial velocities method was used for velocity initialization. The simulation temperature was chosen to represent actual electrochemical environment at room temperature (298 K) and the Nose thermostat served as temperature control method. The simulation was run for a total time of 500 ps, with a timestep of 1.0 fs, until reaching an equilibrium state. The methods of summing the van der Waals interaction and the electrostatic interaction were based on Atom and Ewald, respectively.

3. Results and discussion

3.1. Synthesis and porous structure

By self-assembling of 5-nitroisophthalic acid/isophthalic acid, 4,4'-bipyridine, Zn(II), Ni(II) and Fe(III) ions under solvothermal and stirring conditions, the trimetallic MOF precursors of ZnFeNi-MOF-R (R = NO₂, H) were synthesized (Scheme 1 and Fig. S1). PXRD and FT-IR confirmed that their structures were identical to the reported CID series MOFs with interdigitated construction (Fig. S2 and S3) [38,39]. For comparison, ZnFeNi-MOF-NO₂ with other metal ratios and the bimetallic ZnNi/ZnFe-MOF precursors were also synthesized through similar procedures (Fig. S4). Then, the porous carbon supported FeNi nanoalloys (FeNi@PC-R, R = NO₂, H) were constructed by pyrolyzing the MOF precursors under N₂ atmosphere, where the different organic ligands experience different pyrolysis behaviors to provide carbon and nitrogen sources for generating porous carbon networks. All the samples derived from ZnFeNi-MOF with different functional groups and/or various metal ratios exhibited diffraction peaks at about 74.7°, 50.8° and 43.6°, which represented to (220), (200) and (111) crystal planes of face-centered cubic (fcc) Fe_{0.64}Ni_{0.36} alloy phase (JCPDS No. 47-1405) (Fig. S5 and S6), being different with the monometallic Ni@PC-NO₂ (metallic Ni) and Fe@PC-NO₂ (mixed of Fe and FeC_x) (Fig. S6). FESEM images revealed that FeNi@PC-NO₂ and FeNi@PC-H showed a porous tubular and block-typed morphologies, respectively. It can be seen in the zoomed in areas that lots of mesopore and macropore were formed on FeNi@PC-NO₂, while FeNi@PC-H was relatively dense, with only a spot



Scheme 1. Schematic illustration of the synthesis and structures of trimetallic MOF precursors ZnFeNi-MOF-R ($R = H, NO_2$) and their derived FeNi nanoalloys (represented by golden balls) loaded porous carbons of FeNi@PC-R ($R = H, NO_2$) without or with in situ cavitation.

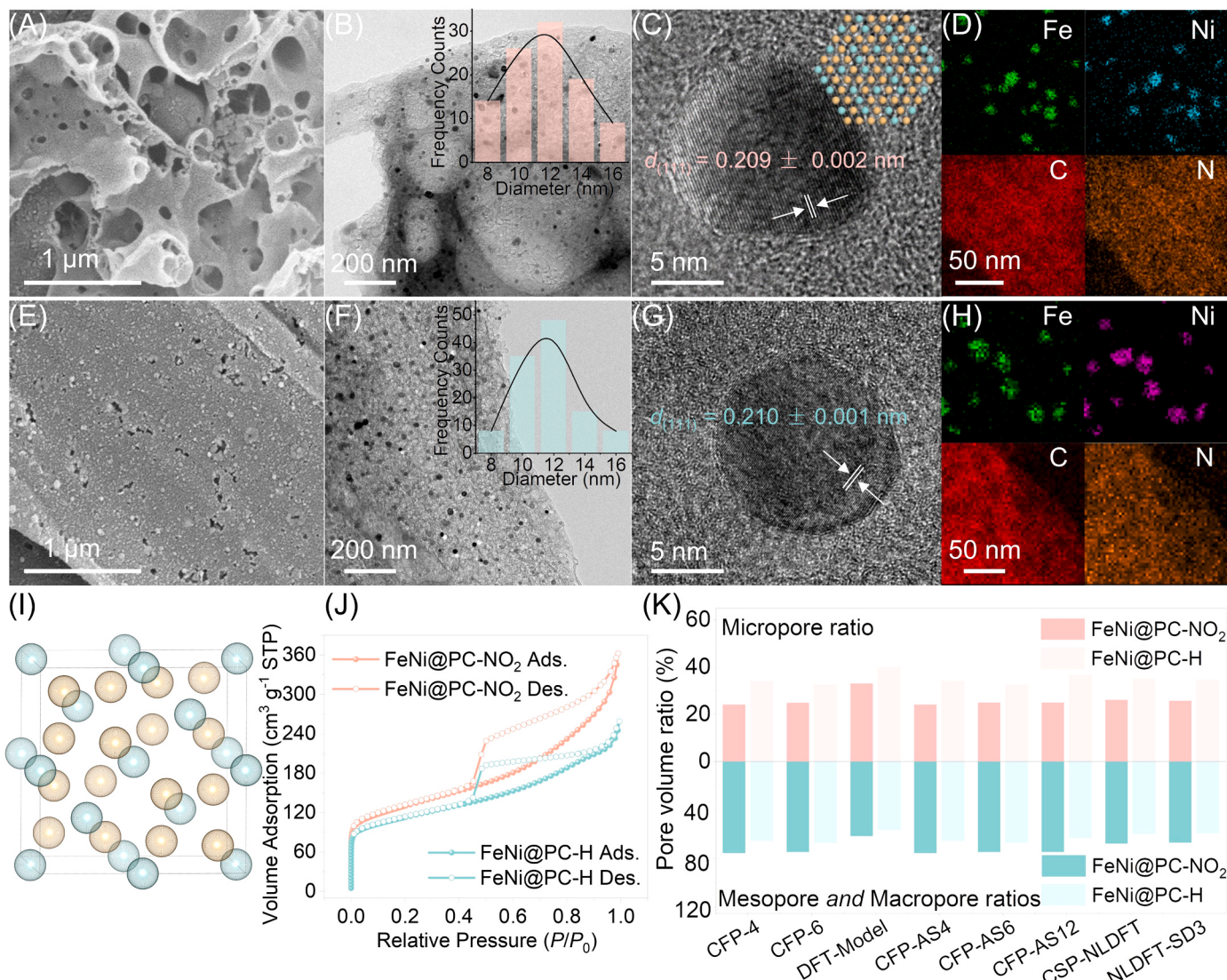


Fig. 1. Morphology, structure and pore characteristics. (A) FESEM, (B) TEM (inset shows the size distribution of nanoalloy particles), (C) HRTEM images (inset is the atomic arrangement on (111) lattice plane of $Fe_{0.64}Ni_{0.36}$ alloy) and (D) the corresponding elemental mapping images of Fe, Ni, C and N of FeNi@PC-NO₂. (E) FESEM, (F) TEM (inset shows the size distribution of nanoalloy particles), (G) HRTEM image, and (H) the corresponding elemental mapping images of Fe, Ni, C and N of FeNi@PC-H. (I) 3D cell model of $Fe_{0.64}Ni_{0.36}$ alloy (Ni: green, Fe: yellow). (J) 77 K N_2 sorption isotherms of FeNi@PC-R ($R = NO_2, H$). (K) Pore volume ratios of micropore or mesopore/macropore in FeNi@PC-R ($R = NO_2, H$) calculated by eight different pore volume analysis methods.

of mesopore on the surface (Fig. 1A and E).

Transmission electron microscopy (TEM) images further confirmed that FeNi@PC-NO₂ possessed a thinner and more porous carbon substrate compared with the nitro-free sample (Fig. 1B and F). These morphological features indicated that gas evolution derived from the nitro groups could conduct *in situ* cavitation to guide the formation of foam-like porous microstructure. FeNi alloy nanoparticles were uniformly distributed on the carbon supports with basically the same average particle-sizes, which are 11.6 ± 1.9 nm and 11.7 ± 2.3 nm, respectively (inset of Fig. 1B and F). The lattice fringes with interplanar spacing of 0.209 ± 0.002 and 0.210 ± 0.001 nm in the high-resolution (HR)TEM images (Figs. 1C and 1G), corresponding to the (111) crystal plane of Fe_{0.64}Ni_{0.36} alloy. The elemental mappings derived from energy dispersive X-ray spectroscopy (EDS) indicated clearly that both FeNi@PC-NO₂ (Fig. 1D) and FeNi@PC-H were composed of C, N, Fe and Ni elements with Fe and Ni concentrated on the nanoparticles (Fig. 1H). Moreover, ICP-OES displayed that Fe and Ni contents in FeNi@PC-NO₂ and FeNi@PC-H were basically the same (Table S1).

Gas adsorption was employed to investigate the samples' specific surface areas and pore structures. The N₂ sorption isotherms showed

obvious hysteresis for all samples, revealing the presence of mesopores (Fig. 1J). FeNi@PC-NO₂ possessed similar BET specific surface area ($467.8 \text{ m}^2 \cdot \text{g}^{-1}$, mainly contributed by micropores) with that of FeNi@PC-H ($405.8 \text{ m}^2 \cdot \text{g}^{-1}$), yet much larger total pore volume ($0.534 \text{ cm}^3 \cdot \text{g}^{-1}$) than that of the latter ($0.343 \text{ cm}^3 \cdot \text{g}^{-1}$). The average pore size distribution of micropores and mesopores were concentrated upon ca. 1–2 and 2–8 nm, respectively (Fig. S7). It is of interest that the micropore ratio and mesopore/macropore ratio were markedly different between two samples. The calculated results based on eight different methods of pore-size distribution analysis showed that the micropore ratio in FeNi@PC-H (average of 35.0%) was obviously larger than that of FeNi@PC-NO₂ (average of 26.2%), while the latter possessed much larger mesopore/macropore ratio (average of 73.8%) than the former (average of 65.0%), being consistent with the morphology characterizations (Fig. 1K). Meanwhile, the BET specific surface areas of Zn-MOF-NO₂, ZnFeNi-MOF-NO₂ and ZnFeNi-MOF-H were 5.1, 10.4 and $9.1 \text{ m}^2 \cdot \text{g}^{-1}$, respectively (Fig. S8 and S9). Such low values indicated that the high porosity as well as much larger BET specific surface areas after carbonization were not caused by the inherent porose structures of the precursors. To exclude the role of Zn in pore engineering, we synthesized

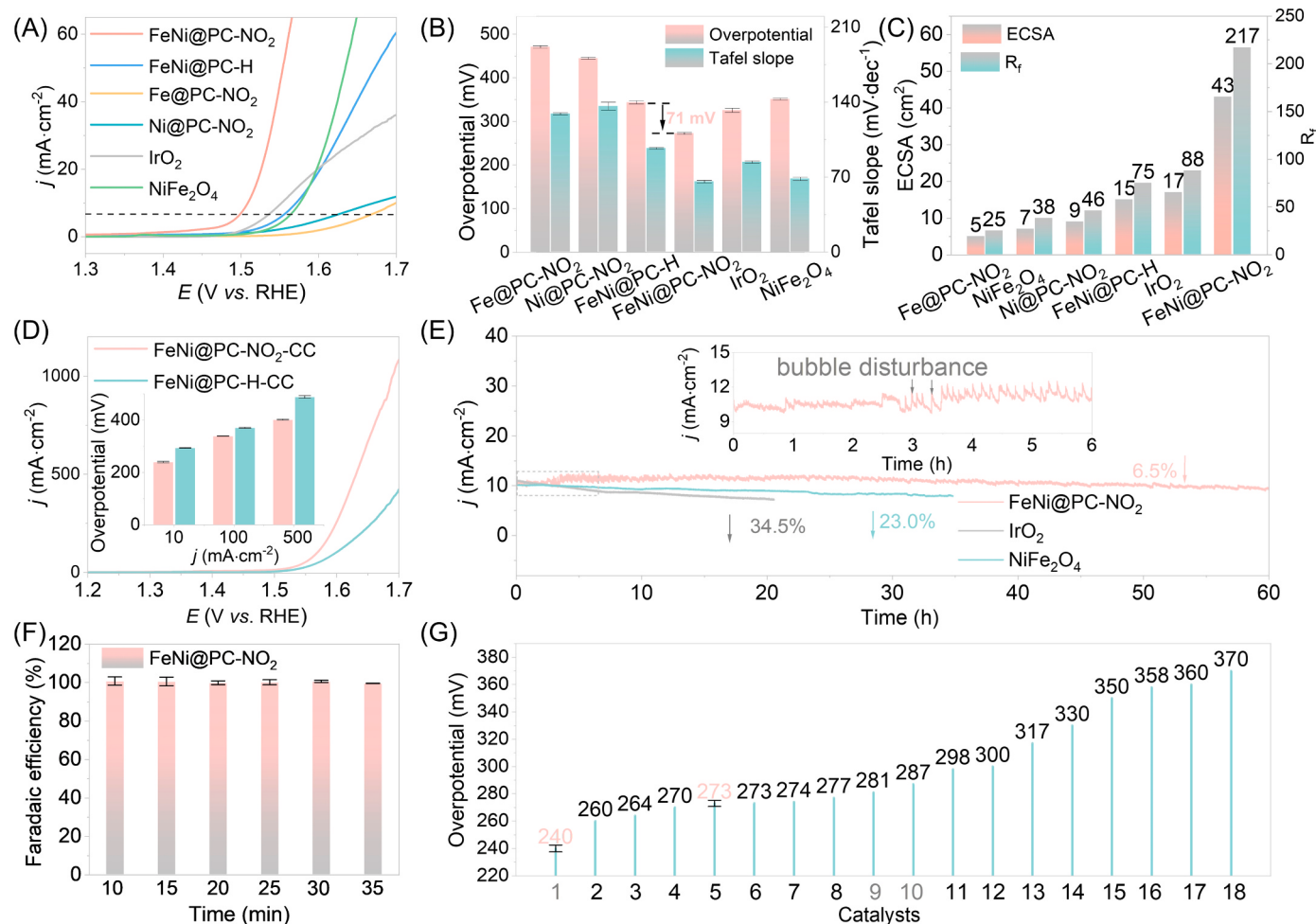


Fig. 2. Oxygen evolution evaluation. (A) OER polarization curves of FeNi@PC-NO₂, FeNi@PC-H, Fe@PC-NO₂, Ni@PC-NO₂, IrO₂ and NiFe₂O₄ in 1.0 M KOH. (B) Overpotentials at $j = 10 \text{ mA} \cdot \text{cm}^{-2}$ and the corresponding Tafel slopes of different catalysts. (C) ECSA and R_f of different catalysts. (D) OER polarization curves of FeNi@PC-NO₂ and FeNi@PC-H on CC in 1.0 M KOH (inset: overpotentials for achieving current densities of 10, 100 and 500 $\text{mA} \cdot \text{cm}^{-2}$, respectively). (E) Chronamperometry curves for FeNi@PC-NO₂, IrO₂ and NiFe₂O₄, the inset shows expanded view of the first 6 h for FeNi@PC-NO₂. (F) Faraday efficiency under different electrolysis times for FeNi@PC-NO₂. (G) Comparisons of the overpotentials at $j = 10 \text{ mA} \cdot \text{cm}^{-2}$ on GCE and CC of the advanced FeNi alloy-based electrocatalysts (the gray label represents the performance on CC). The catalysts name from 1 to 18 are FeNi@PC-NO₂-CC, Ni₃Fe@N-C [40], FeNi₃ @NCNT [41], NDCHN-35 [42], FeNi@PC-NO₂-GCE, Fe-Ni@NC(1/2)-800 [43], NiFe@C [44], FeNi₃ @NC [45], NiFe@OCC [46], NiFe_{0.5}A [47], FeNi@NC-nanosphere [48], Ni₃Fe nitride [49], FeNi-NCF-800 [50], Ni_{0.9}Fe_{0.1}/NC [51], FeNi/NC [52], NiFe-DG [53], NC-NiFe [54], and NiFe alloy [55], respectively (detailed comparison parameters can be found in the list of supplementary information). Error bars on data points were calculated from three experimental repetitions.

CoFeNi@PC-NO₂ and CoFeNi@PC-H as controls by replacing Zn with Co (Fig. S10 A and B). By testing their BET specific surface area and calculating the corresponding pore size distribution, the results showed that the micropore proportion of FeNi@PC-H (22.4%) was larger than that of FeNi@PC-NO₂ (13.6%). However, the latter had a higher proportion of macropores/mesopores (86.4%) compared with the former (77.6%) (Fig. S10 C and D). These results supported the significant role of nitro-substituted organic ligands in the pore regulation of porous carbon matrix. The higher I_D/I_G intensity ratio in Raman spectra (Fig. S11) indicated more defective graphite structure in FeNi@PC-NO₂, also reflecting the more highly porous structure through in situ cavitation.

3.2. Electrocatalytic performance

To evaluate the catalytic OER performance of the prepared catalysts, linear sweep voltammetry (LSV) was carried out in a 1.0 M KOH electrolyte solution. After systematically optimizing the metal ratios in the catalyst and total loading amounts on GCE (Fig. S13), we can find that FeNi@PC-NO₂ required only a low overpotential of 272.5 ± 2.2 mV to drive a current density of $10 \text{ mA}\cdot\text{cm}^{-2}$ (Fig. 2A and Fig. S14), much lower than those of FeNi@PC-H (343.7 ± 3.6 mV), Ni@PC-NO₂ (444.5 ± 2.3 mV), Fe@PC-NO₂ (470.8 ± 2.5 mV), and commercial IrO₂ (325.7 ± 4.7 mV). In order to better compare the catalytic activity of catalysts under alkaline conditions, we synthesized NiFe₂O₄ as the reference material (Fig. S15), which exhibited an overpotential of 351.0 ± 2.0 mV at $10 \text{ mA}\cdot\text{cm}^{-2}$ and a Tafel slope of $68.3 \pm 1.5 \text{ mV}\cdot\text{dec}^{-1}$. Compared to NiFe₂O₄, FeNi@PC-NO₂ displayed remarkably superior catalytic activity (272.5 ± 2.2 mV and $65.7 \pm 1.1 \text{ mV}\cdot\text{dec}^{-1}$). Moreover, FeNi@PC-NO₂ showed remarkably lower Tafel slope of $65.7 \pm 1.1 \text{ mV}\cdot\text{dec}^{-1}$ compared with FeNi@PC-H ($96.8 \pm 0.8 \text{ mV}\cdot\text{dec}^{-1}$) and other reference catalysts, indicating that it had more rapid oxygen evolution kinetics (Fig. 2B). By measuring the double-layer capacitance (C_{dl}) of CV at various scan rates in the non-Faraday region, ECSA and R_f of each catalyst were estimated. (Fig. S16). The results showed that FeNi@PC-NO₂ should possess higher active surface as it displayed the largest ECSA and R_f value than those of FeNi@PC-H and other reference catalysts (Fig. 2C) [35–37], being consistent with the pore characteristics. The charge transfer properties of the catalysts was assessed using EIS. The charge-transfer resistance of FeNi@PC-NO₂ ($R_{CT} = 48.8 \Omega$) was significantly smaller than those of other catalysts, revealing its higher electron transfer ability (Fig. S17). The conductivity test results indicated that FeNi@PC-NO₂ exhibited superior conductivity to FeNi@PC-H (Table S2). Moreover, as shown in Fig. 2D, FeNi@PC-NO₂ on carbon cloth (CC) afforded 239.6 ± 2.5 , 339.0 ± 1.0 , and 401.6 ± 2.1 mV to deliver the current densities of 10, 100 and $500 \text{ mA}\cdot\text{cm}^{-2}$, respectively, being superior to FeNi@PC-H (294.0 ± 1.0 , 371.3 ± 2.5 and 489.5 ± 4.9 mV). In addition, compared with IrO₂ and NiFe₂O₄, FeNi@PC-NO₂ exhibited excellent electrocatalytic durability with just 6.5% decrease of the current density after 60 h electrolysis (Fig. 2E), and kept the Faradaic efficiency as high as 99% (Fig. 2F). At the same time, the long-term stability of this electrocatalyst was also confirmed by the PXRD and TEM measurements after OER (Fig. S18, S19). It can be seen that FeNi@PC-NO₂ possesses superior OER performance among the recently reported FeNi nanoalloy-based electrocatalysts (Fig. 2G). In order to evaluate the potential application of FeNi@PC-NO₂, we constructed an anion exchange membrane (AEM) electrolyzer cell catalyzed by Pt/C||FeNi@PC-NO₂. In 1 M KOH, at a cell voltage of 2.0 V, the current density of the AEM electrolyzer cell can reach $1.2 \text{ A}\cdot\text{cm}^{-2}$, while the current density of Pt/C||NiFe₂O₄ under the same applied voltage is only $0.7 \text{ A}\cdot\text{cm}^{-2}$ (Fig. S20).

3.3. Electrocatalytic enhancement mechanism

The surface chemical composition and elemental valence state of the catalyst were analyzed using XPS. The results displayed that both the

binding energies of Fe 2p and Ni 2p in FeNi@PC-NO₂ and FeNi@PC-H showed negligible changes, which should be due to their almost indistinguishable alloyed phases, metal contents/ratios, nanoparticle sizes, and meanwhile indicating the pore-structure difference of the carbon supports does not significantly affect the electronic structure of metal nanoalloys (Fig. 3A and B). In addition, the identical high-resolution C 1 s, N 1 s and O 1 s spectra of FeNi@PC-NO₂ and FeNi@PC-H further revealed that the chemical states of their carbon supports were basically consistent (Fig. 3C, D and E) [56,57]. Some previous researches have shown that the pre-oxidation or surface reconstruction of electrocatalysts plays a significant role in the evaluation of real active substances for OER [58,59]. CV test (Fig. 3F) and HRTEM image (Fig. 3G) showed that the surface of FeNi@PC-NO₂ was activated during electrocatalysis and reconstituted to form the core-shell structure with amorphous FeNi-oxyhydroxide layer outside the surface of FeNi nanoalloy, which could give a better balance between the exposing active sites and the electron transfer [60]. The XPS analysis shows that after OER, the peaks of Fe³⁺ and Ni²⁺ were both shifted to higher binding energies due to anodic oxidation, which has been widely observed in nanoalloy OER electrocatalysts (Fig. S21, S22) [61,62]. Furthermore, it was clearly observed that the binding energies of Fe⁰ and Ni⁰ in FeNi@PC-R (R = NO₂, H) were positively and negatively shifted by 0.32 eV and 1.4 eV compared with those of Fe@PC-NO₂ and Ni@PC-NO₂, respectively, which demonstrated that partial electrons were transfer from Fe to Ni in the bimetal alloys (Fig. S21, S22).

DFT calculations were employed to illustrate the potential electrocatalytic mechanism as well as synergistic effect of FeNi bimetals. Based on the above electrocatalytic and HRTEM results, periodic surface models of FeOOH, NiOOH, and Fe₂NiOOH (Fe/Ni ratio of 2/1) were adopted for the calculations. According to the typical four-electron mechanism of OER (Fig. 3H), the Gibbs free energy diagram of each catalyst was calculated. It showed that the more favorable active site is Fe in Fe₂NiOOH, and the rate-determining step is the formation of OOH intermediate with an energy barrier of $\Delta G_3 = 1.68$ eV. Obviously, the rate-determining energy barrier on Fe₂NiOOH was significantly lower than those on FeOOH ($\Delta G_3 = 2.28$ eV) and NiOOH ($\Delta G_2 = 2.12$ eV), indicating that the synergistic effect between Fe and Ni remarkably facilitates OER kinetics (Fig. 3I).

In order to illustrate the influence of different pore structures on the mass transfer, we performed molecular dynamics (MD) simulations to investigate the diffusion behaviors of H₂O molecules in different carbon-based pores. A confined space surrounded by two layers of graphene with distance of 10 or 30 Å was constructed to simulate micropore or mesopore, respectively. Then, H₂O molecules with a density of $1.0 \text{ g}\cdot\text{cm}^{-3}$ were filled in the confined interlayer pores (Fig. 4A and B). After 500 ps MD simulation, the theoretical diffusion coefficient of H₂O molecule was calculated from the root mean square (RMS) displacement plots. As expected, the theoretical diffusion coefficient of H₂O in the 30 Å mesopore model ($33.9 \times 10^{-9} \text{ m}^2\cdot\text{s}^{-1}$) was almost 5 times higher than that in the 10 Å micropore model ($6.8 \times 10^{-9} \text{ m}^2\cdot\text{s}^{-1}$), demonstrating that the mass transfer of H₂O can be significantly improved in mesopores (Fig. 4C). For comparison, we also used periodic boxes with heights of 30 and 10 Å loading with identical densities of H₂O to simulate the diffusion of free H₂O molecules without carbon confinement (Fig. S23 and S24). The results showed that the box-size exhibited very small influence on the free H₂O diffusion, both with relatively smaller theoretical diffusion coefficients (3.9×10^{-9} and $3.4 \times 10^{-9} \text{ m}^2\cdot\text{s}^{-1}$, respectively). The faster diffusion in the confinement carbon space indicates that the interaction between the pore wall and H₂O molecules could significantly promote the guest molecule motion. However, pore size should be a non-negligible parameter, and mesopore can be more favorable to the diffusion of guest as well as mass transfer. In order to further prove our conclusion, the diffusion coefficients were measured by the linearization of the falling part of the transients through Cottrell equation [63,64]:

$$j = nFcD^{1/2}\pi^{-1/2}t^{-1/2}.$$

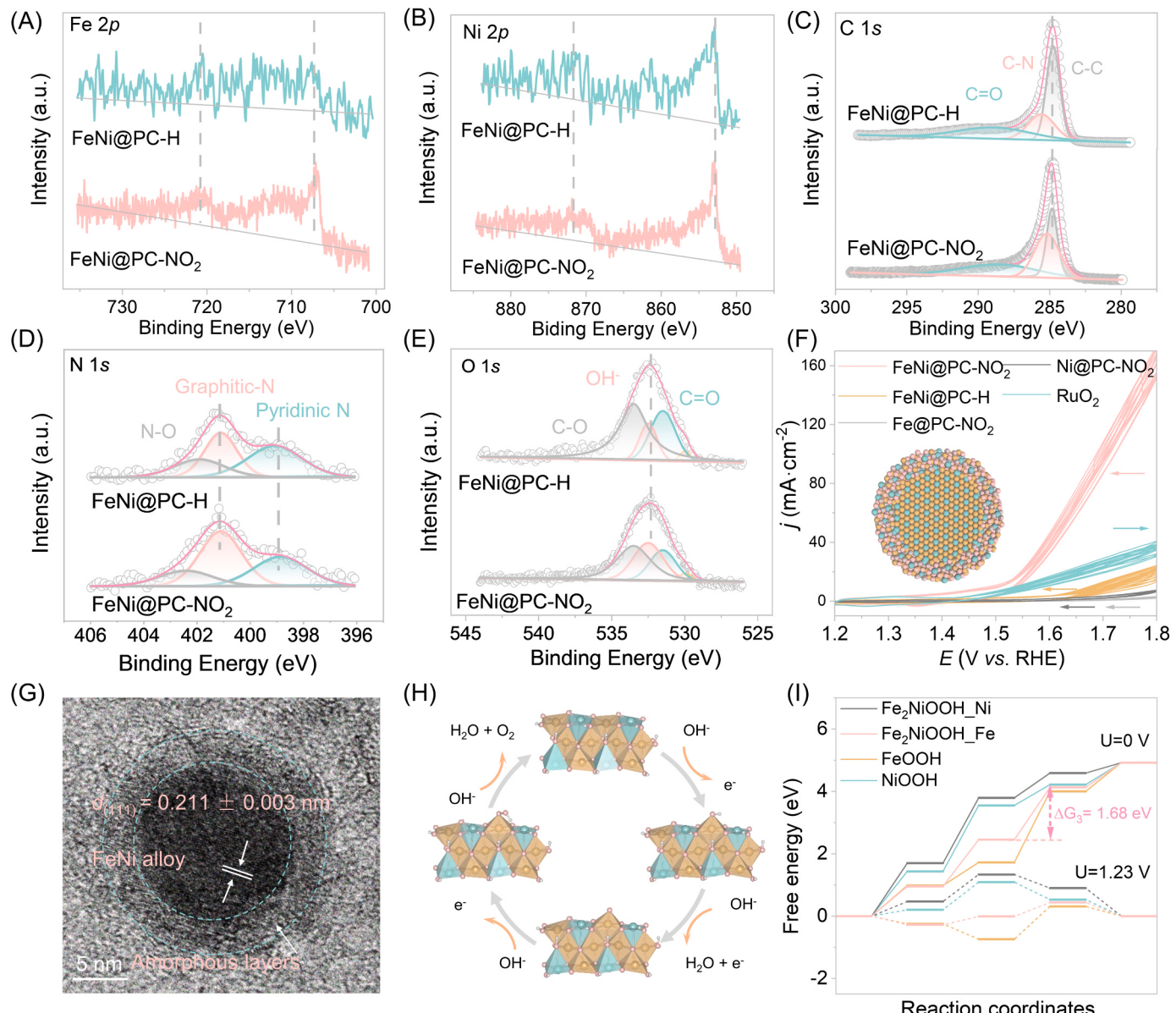


Fig. 3. Surface reconstruction and bimetal synergy. XPS spectra of (A) Fe 2p, (B) Ni 2p (C) C 1 s, (D) N 1 s and (E) O 1 s in FeNi@PC-H and FeNi@PC-NO₂, respectively. (F) CV activation of different catalysts in 1.0 M KOH and the arrows indicate the direction in which each CV curve changes (inset: schematic diagram of Fe_{0.64}Ni_{0.36} alloy covered with amorphous oxide layer after OER reaction). (G) HRTEM image of FeNi@PC-NO₂ after OER electrocatalysis. (H) Four-electron-transferred OER mechanism diagram with optimized configurations of intermediates for FeNi@PC-NO₂. (I) Gibbs free energy diagrams for OER on FeOOH, NiOOH, and Fe₂NiOOH surface models.

nF is the molar charge transferred during the electrochemical process, t is the time, c is the reduced state concentration and D is the diffusion coefficient. By measuring the $i-t$ transient curve (Fig. S25), the diffusion coefficient can be calculated from the slope of the j vs. $t^{-1/2}$ plot. It is worth noting that the Cottrell equation can be the criterion to test whether the reaction is controlled by diffusion. If a straight line through the origin is obtained, the reaction is mainly controlled by diffusion [65]. Our measurements met this requirement (Fig. 4D), and showing that the diffusion coefficient of FeNi@PC-NO₂ ($5.6 \times 10^{-9} \text{ m}^2 \cdot \text{s}^{-1}$) is much higher than that of FeNi@PC-H ($0.62 \times 10^{-9} \text{ m}^2 \cdot \text{s}^{-1}$), which indicates faster mass transfer in the former catalyst. A high-speed camera was used to record the OER process for comparing the size distribution and releasing rate of gas bubbles (Fig. 4E-H). The average sizes of the releasing bubbles from FeNi@PC-NO₂ and FeNi@PC-H electrodes were 210 and 330 μm , respectively, indicating the much faster re-exposure of catalytic sites to the surrounding electrolyte for

FeNi@PC-NO₂ [66]. Moreover, the surface wettability under electrolyte of the as-prepared electrodes was investigated by contact-angle measurement in 1 M KOH (Fig. 4I and J). The water-droplet contact-angle on FeNi@PC-NO₂ and FeNi@PC-H were 71.6° and 126.7°, respectively, confirming better reactant affinity of FeNi@PC-NO₂ [67]. These results were consistent with the above-mentioned porous structures and electrocatalytic performances.

To further verify the universality of the in situ cavitation strategy, other two groups of metal-carbon composites derived from different types of MOFs with and without nitro modification were synthesized. The two groups of MOF precursors were ZIF-67/ ZIF-67-NO₂ and Co-BDC/Co-BDC-NO₂ (Fig. S26 and S27), and their corresponding derivatives were denoted as Co@PC-1/Co@PC-NO₂-1 and Co@PC-2/Co@PC-NO₂-2, respectively. PXRD patterns confirmed that Co nanoparticles were obtained after pyrolysis (Fig. S28). FE-SEM images showed more porous and rougher on the surface through the cavitation

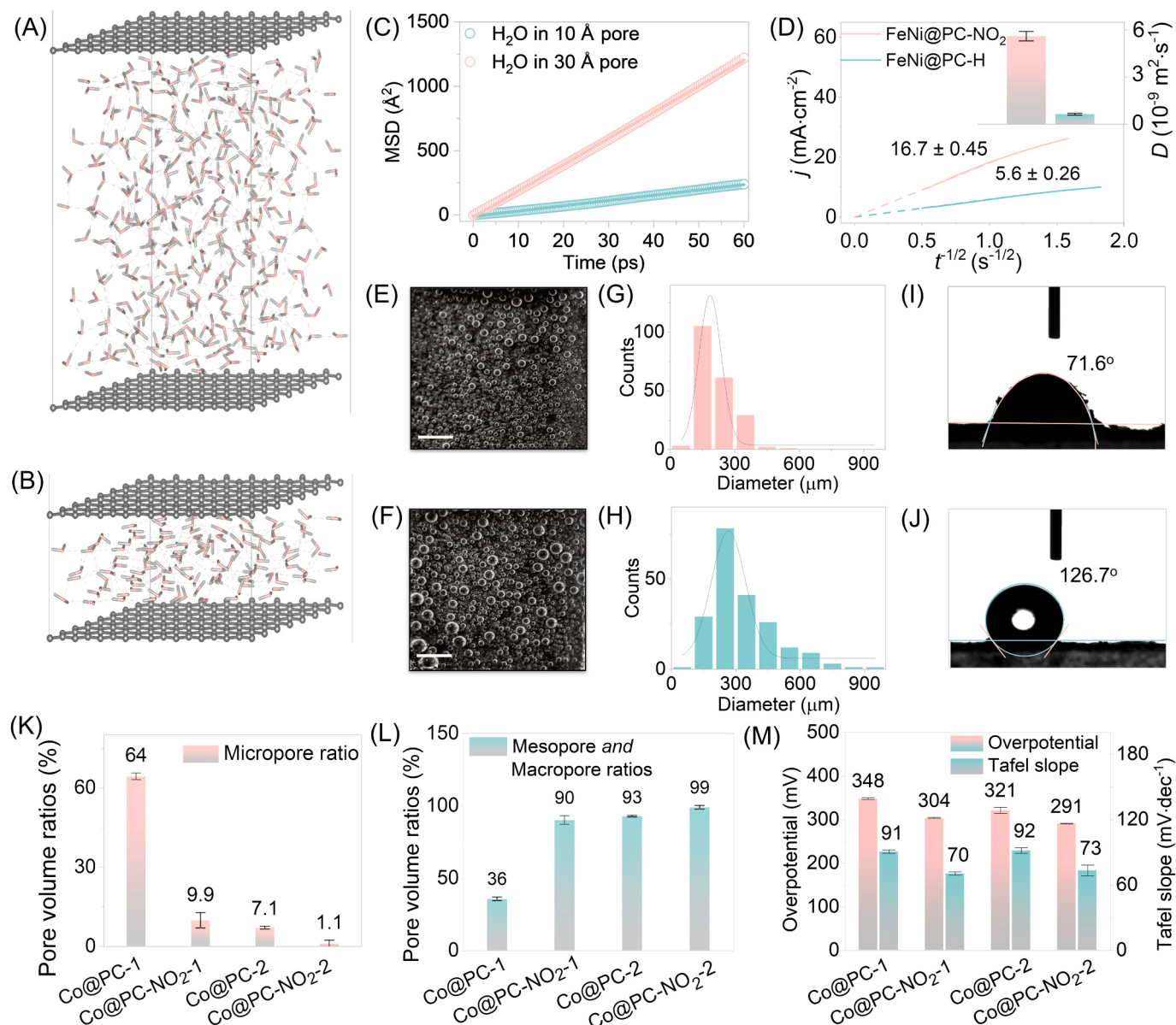


Fig. 4. Mass transfer regulated by pore structures. (A) 30 Å and (B) 10 Å carbon-based pore models filled with water molecules (density of 1.0 g·cm⁻³). (C) RMS displacement plots of water molecules in 30 Å and 10 Å carbon-based pore, respectively. (D) Slopes and diffusion coefficients (inset) calculated by Cottrell equation at overpotential of 270 mV. (E and F) Photographs of bubbles released on the electrode surface of FeNi@PC-NO₂ and FeNi@PC-H for OER at a current density of 200 mA·cm⁻² (scale bars: 2 mm). (G and H) Corresponding size distributions of the releasing bubbles based on two hundred bubbles. (I and J) Water-droplet contact angles for FeNi@PC-NO₂ and FeNi@PC-H, respectively. (K and L) Pore volume ratios (error bar calculated from eight different pore volume analysis results) of micropore or mesopore/macropore in Co@PC-1, Co@PC-NO₂-1, Co@PC-2, and Co@PC-NO₂-2, respectively. (M) Overpotentials at $j = 10 \text{ mA}\cdot\text{cm}^{-2}$ and Tafel slopes of Co@PC-1, Co@PC-NO₂-1, Co@PC-2, and Co@PC-NO₂-2. Error bars on data points were calculated from three experimental repetitions.

by nitro group (Fig. S29). Interestingly, both the BET specific surface areas (60.2 and $25.6 \text{ m}^2\cdot\text{g}^{-1}$) of the catalysts derived from nitro-modified MOFs were smaller than those (467.4 and $34.3 \text{ m}^2\cdot\text{g}^{-1}$) of the corresponding nitro-free counterparts (Fig. S30, S31). According to the above eight algorithms for calculating pore size distribution, after the introduction of nitro group to the MOF precursors, the micropore ratios decreased significantly from $64.3 \pm 1.2\%$ / $7.2 \pm 0.5\%$ to $9.9 \pm 2.9\%$ / $1.1 \pm 1.2\%$, respectively. In contrast, the ratio of mesopores/macropores increased from $35.7 \pm 1.2\%$ / $92.8 \pm 0.5\%$ to $90.1 \pm 2.9\%$ / $98.9 \pm 1.2\%$, respectively (Fig. 4K and L). Due to these changes of pore structures on the carbon supports, Co@PC-NO₂-1 and Co@PC-NO₂-2 both exhibited markedly lower OER overpotentials of 303.7 ± 1.3 mV and 291.0 ± 0.7 mV at $10 \text{ mA}\cdot\text{cm}^{-2}$, compared with those of nitro-free counterparts, respectively (Fig. S32). Meanwhile, the corresponding

Tafel slopes decreased from 90.7 ± 1.5 and $91.7 \pm 2.5 \text{ mV}\cdot\text{dec}^{-1}$ to 70.5 ± 1.5 and $73.3 \pm 4.9 \text{ mV}\cdot\text{dec}^{-1}$, respectively (Fig. 4M), indicating the remarkably improved oxygen evolution kinetics after enhancing the mesopores/macropore ratio. These results once again demonstrated that nitro modification in the precursors could significantly tune the pore structure of the derived porous carbon matrix, and then effectively facilitate mass transfer and adequate contact of reactants with catalytic sites during electrocatalysis.

4. Conclusion

In summary, we have developed a universal strategy to modulate the pore structures of nanoparticle-loaded carbon materials by using nitro modification on the molecule-based precursors. Gas sorption

measurements and MD simulations revealed that the mesopore and macropore ratio of the carbon support can be significantly increased through the in situ cavitation during carbonization process, which tellingly promote the mass transfer as well as gas evolution kinetics. In addition, this pore regulation method for catalyst support does not significantly affect the electronic structures of metal species, so it is compatible with conventional electronic structure regulation strategies. Specifically, the prepared FeNi@PC-NO₂ with modest-size FeNi nanoalloys loading on foam-like carbon exhibited improved OER performance with overpotentials of 272.5 ± 2.2 mV on GCE and 239.6 ± 2.5 mV on CC at the current density of $10 \text{ mA} \cdot \text{cm}^{-2}$, surpassing its nitro-free counterpart, benchmarking RuO₂ and other reported FeNi alloy-based electrocatalysts. Our work provides a new insight into the catalyst support for improving the performance of electrocatalysts. Moreover, the thought of side-group regulation on molecule-based precursors should have broad prospects in the renewable energy catalysis and conversion systems.

CRediT authorship contribution statement

C.-T. H. conceived the idea, designed the study, and guided the project. H.-G. D., X.-F. Z. and J.-L. L. performed the experiments and most of the data analysis. C.-T. H. and X.-F. Z. conducted theoretical calculations. L.-W. D., L.-H. Y., X.-H. Z., L.-M. C., and J. Z. joined the discussion of data and gave useful suggestions. C.-T. H., H.-G. D., Y. D. and J.-L. L. drafted the manuscript. All authors discussed and commented on the manuscript.

Declaration of Competing Interest

The authors declare that they have no known competing financial interests or personal relationships that could have appeared to influence the work reported in this paper.

Data Availability

Data will be made available on request.

Acknowledgements

This work was supported by the National Natural Science Foundation of China (22161021, 22375079, 32101750), and the Natural Science Foundation of Jiangxi Province (20224ACB214001). Y. D. acknowledges the Oversea Leading Talent of Shanghai. C.-T. H. acknowledges the support of Jiangxi Province (jxsq2018106041).

Appendix A. Supporting information

Supplementary data associated with this article can be found in the online version at [doi:10.1016/j.apcatb.2023.123396](https://doi.org/10.1016/j.apcatb.2023.123396).

References

- [1] Z.-Y. Yu, Y. Duan, X.-Y. Feng, X. Yu, M.-R. Gao, S.-H. Yu, Clean and affordable hydrogen fuel from alkaline water splitting: past, recent progress, and future prospects, *Adv. Mater.* 33 (2021) 2007100, <https://doi.org/10.1002/adma.202007100>.
- [2] Y. Zhang, X. Shen, C. Song, Z. Ji, F.-H. Du, Sulfur-doped NiFe(CN)₂NO nanoparticles as efficient electrocatalysts for the oxygen evolution reaction, *J. Mater. Chem. A* 11 (2023) 8904–8911, <https://doi.org/10.1039/D3TA00635B>.
- [3] Modulating electronic structure of metal–organic framework derived catalysts for electrochemical water oxidation, in: B. Singh, A. Singh, A. Yadav, A. Indra (Eds.), *Coord. Chem. Rev.*, 447, 2021, 214144, <https://doi.org/10.1016/j.ccr.2021.214144>.
- [4] X. Liu, X. Zhao, S. Cao, M. Xu, Y. Wang, W. Xue, J. Li, Local hydroxyl enhancement design of NiFe sulfide electrocatalyst toward efficient oxygen evolution reaction, *Appl. Catal., B* 331 (2023), 122715, <https://doi.org/10.1016/j.apcatb.2023.122715>.
- [5] Z.-Y. Wu, P. Zhu, D.A. Cullen, Y. Hu, Q.-Q. Yan, S.-C. Shen, F.-Y. Chen, H. Yu, M. Shakouri, J.D. Arregui-Mena, A. Ziabari, A.R. Paterson, H.-W. Liang, H. Wang, A general synthesis of single atom catalysts with controllable atomic and mesoporous structures, *Nat. Synth. 1* (2022) 658–667, <https://doi.org/10.1038/s44160-022-00129-x>.
- [6] Q. Lu, X. Zou, Y. Biu, Z. Shao, Structural design of supported electrocatalysts for rechargeable Zn-air batteries, *Energy Storage Mater.* 55 (2022) 166–192, <https://doi.org/10.1016/j.ensm.2022.11.046>.
- [7] J. Quílez-Bermejo, S. García-Dalí, A. Daouli, A. Zitolo, R.L.S. Canevesi, M. Emo, M. T. Izquierdo, M. Badawi, A. Celzard, V. Pierro, Advanced design of metal nanoclusters and single atoms embedded in C₁N₁-derived carbon materials for ORR, HER, and OER, *Adv. Funct. Mater.* 33 (2023) 2300405, <https://doi.org/10.1002/adfm.202300405>.
- [8] L.-M. Cao, J. Zhang, X.-F. Zhang, C.-T. He, Confinement synthesis in porous molecule-based materials: a new opportunity for ultrafine nanostructures, *Chem. Sci.* 13 (2022) 1569–1593, <https://doi.org/10.1039/D1SC05983A>.
- [9] M. Li, Y. Yang, D. Yu, W. Li, X. Ning, R. Wan, H. Zhu, J. Mao, Recent advances on the construction of encapsulated catalyst for catalytic applications, *Nano Res.* 16 (2023) 3451–3474, <https://doi.org/10.1007/s12274-022-4859-4>.
- [10] Y. Li, M. Lu, Y. Wu, Q. Ji, H. Xu, J. Gao, G. Qian, Q. Zhang, Morphology regulation of metal–organic framework-derived nanostructures for efficient oxygen evolution electrocatalysis, *J. Mater. Chem. A* 8 (2020) 18215–18219, <https://doi.org/10.1039/DOTA05866A>.
- [11] L. Huang, G. Gao, H. Zhang, J. Chen, Y. Fang, S. Dong, Self-dissociation-assembly of ultrathin metal–organic framework nanosheet arrays for efficient oxygen evolution, *Nano Energy* 68 (2020), 104296, <https://doi.org/10.1016/j.nanoen.2019.104296>.
- [12] F. Pan, T. Jin, W. Yang, H. Li, Y. Cao, J. Hu, X. Zhou, H. Liu, X. Duan, Theory-guided design of atomic Fe–Ni dual sites in N,P-co-doped C for boosting oxygen evolution reaction, *Chem. Catal.* 1 (2021) 734–745, <https://doi.org/10.1016/j.jchcat.2021.06.017>.
- [13] G. Zhang, X. Liu, X. Zhang, Z. Liang, G. Xing, B. Cai, D. Shen, L. Wang, H. Fu, Phosphate-decorated Fe-N-C to promote electrocatalytic oxygen reaction activities for highly stable zinc-air batteries, *Chin. J. Catal.* 49 (2023) 141–151, [https://doi.org/10.1016/S1872-2067\(23\)64432-8](https://doi.org/10.1016/S1872-2067(23)64432-8).
- [14] L. Liu, A. Corma, Bimetallic sites for catalysis: from binuclear metal sites to bimetallic nanoclusters and nanoparticles, *Chem. Rev.* 123 (2023) 4855–4933, <https://doi.org/10.1021/acs.chemrev.2c00733>.
- [15] J. Chen, F. Cheng, S.-J. Zhang, A. Fisher, Y. Zhou, Z. Wang, Y. Li, B.-B. Xu, J.-T. Li, S.-G. Sun, Interfacial interaction between FeOOH and Ni–Fe LDH to modulate the local electronic structure for enhanced OER electrocatalysis, *ACS Catal.* 8 (2018) 11342–11351, <https://doi.org/10.1021/acscatal.8b03489>.
- [16] Q. Wang, M. Chen, C. Xiong, X. Zhu, C. Chen, F. Zhou, Y. Dong, Y. Wang, J. Xu, Y. Li, J. Liu, H. Zhang, B. Ye, H. Zhou, Y. Wu, Dual confinement of high-loading enzymes within metal–organic frameworks for glucose sensor with enhanced cascade biocatalysis, *Biosens. Bioelectron.* 196 (2022), 113695, <https://doi.org/10.1016/jbios.2021.113695>.
- [17] J. Yang, B. Yin, S. Zhang, Y. Sun, J. Li, D. Su, T. Ma, Macromolecules promoting robust zinc anode by synergistic coordination effect and charge redistribution, *Small* (2023) 2304913, <https://doi.org/10.1002/smll.202304913>.
- [18] C. Li, E. Zhou, Z. Yu, H. Liu, M. Xiong, Tailor-made open porous 2D CoFe/SN-carbon with slightly weakened adsorption strength of ORR/OER intermediates as remarkable electrocatalysts toward zinc-air batteries, *Appl. Catal., B* 269 (2020), 118771, <https://doi.org/10.1016/j.apcatb.2020.118771>.
- [19] J. Luo, X. Wang, Y. Gu, S. Wang, Y. Li, T. Wang, Y. Liu, Y. Zhou, J. Zhang, Hierarchical sheet-like W-doped NiCo₂O₄ spinel synthesized by high-valence oxanion exchange strategy for highly efficient electrocatalytic oxygen evolution reaction, *Chem. Eng. J.* 472 (2023), 144839, <https://doi.org/10.1016/j.cej.2023.144839>.
- [20] J. Sun, S.K. Sinha, A. Khammari, M. Picher, M. Terrones, F. Banhart, The amorphization of metal nanoparticles in graphitic shells under laser pulses, *Carbon* 161 (2020) 495–501, <https://doi.org/10.1016/j.carbon.2020.01.067>.
- [21] X. Xu, T. Yang, Q. Zhang, W. Xia, Z. Ding, K. Eid, A.M. Abdullah, M. Shahriar, A. Hossain, S. Zhang, J. Tang, L. Pan, Y. Yamauchi, Ultrahigh capacitive deionization performance by 3D interconnected MOF-derived nitrogen-doped carbon tubes, *Chem. Eng. J.* 390 (2020), 124493, <https://doi.org/10.1016/j.cej.2020.124493>.
- [22] W. Wang, X. Xu, W. Zhou, Z. Shao, Recent progress in metal–organic frameworks for applications in electrocatalytic and photocatalytic water splitting, *Adv. Sci.* 4 (2017) 1600371, <https://doi.org/10.1002/advs.201600371>.
- [23] L.-M. Cao, J. Zhang, L.-W. Ding, Z.-Y. Du, C.-T. He, Metal–organic frameworks derived transition metal phosphides for electrocatalytic water splitting, *J. Energy Chem.* 68 (2022) 494–520, <https://doi.org/10.1016/j.jechem.2021.12.006>.
- [24] W. Xiong, H. Li, H. You, M. Cao, R. Cao, Encapsulating metal organic framework into hollow mesoporous carbon sphere as efficient oxygen bifunctional electrocatalyst, *Natl. Sci. Rev.* 7 (2019) 609–619, <https://doi.org/10.1093/nsr/nwz166>.
- [25] Z. Qian, R. Zhang, Y. Xiao, H. Huang, Y. Sun, Y. Chen, T. Ma, X. Sun, Trace to the source: self-tuning of MOF photocatalysts, *Adv. Energy Mater.* 13 (2023) 2300086, <https://doi.org/10.1002/aenm.202300086>.
- [26] K. Wang, Y. Li, L.-H. Xie, X. Li, J.-R. Li, Construction and application of base-stable MOFs: a critical review, *Chem. Soc. Rev.* 51 (2022) 6417–6441, <https://doi.org/10.1039/D1CS00891A>.
- [27] Recent advances in MOFs/MOF derived nanomaterials toward high-efficiency aqueous zinc ion batteries, in: T. Zhao, H. Wu, X. Wen, J. Zhang, H. Tang, Y. Deng, S. Liao, X. Tian (Eds.), *Coord. Chem. Rev.*, 468, 2022, 214642, <https://doi.org/10.1016/j.ccr.2022.214642>.

[28] J. Yang, F. Zhang, X. Wang, D. He, G. Wu, Q. Yang, X. Hong, Y. Wu, Y. Li, Porous molybdenum phosphide nano-octahedrons derived from confined phosphorization in UIO-66 for efficient hydrogen, *Evol. Angew. Chem. Int. Ed.* 55 (2016) 12854–12858, <https://doi.org/10.1002/anie.201604315>.

[29] Tackling orientation of metal-organic frameworks (MOFs): The quest to enhance MOF performance, in: I.E. Khalil, J. Fonseca, M.R. Reithofer, T. Eder, J.M. Chin (Eds.), *Coord. Chem. Rev.*, 481, 2023, 215043, <https://doi.org/10.1016/j.ccr.2023.215043>.

[30] L. Yang, X. Zeng, W. Wang, D. Cao, Recent progress in MOF-derived, heteroatom-doped porous carbons as highly efficient electrocatalysts for oxygen reduction reaction in fuel cells, *Adv. Funct. Mater.* 28 (2018) 1704537, <https://doi.org/10.1002/adfm.201704537>.

[31] E.A. Dolgopolova, A.J. Brandt, O.A. Ejegbawo, A.S. Duke, T. D. Maddumapatabandi, R.P. Galhenage, B.W. Larson, O.G. Reid, S.C. Ammal, A. Heyden, M. Chandrashekhar, V. Stavila, D.A. Chen, N.B. Shustova, Electronic properties of bimetallic metal-organic frameworks (MOFs): tailoring the density of electronic states through MOF modularity, *J. Am. Chem. Soc.* 139 (2017) 5201–5209, <https://doi.org/10.1021/jacs.7b01125>.

[32] A. Wang, C. Zhao, M. Yu, W. Wang, Trifunctional Co nanoparticle confined in defect-rich nitrogen-doped graphene for rechargeable Zn-air battery with a long lifetime, *Appl. Catal., B* 281 (2021), 119514, <https://doi.org/10.1016/j.apcatb.2020.119514>.

[33] K. Kongpatpanich, S. Horike, N. Y.-i. Fujiwara, H. Ogiwara, S. Nishihara, Kitagawa, Formation of foam-like microstructural carbon material by carbonization of porous coordination polymers through a ligand-assisted foaming process, *Chem. Eur. J.* 21 (2015) 13278–13283, <https://doi.org/10.1002/chem.201501988>.

[34] F. Rong, J. Zhao, Q. Yang, C. Li, Nanostructured hybrid NiFeOOH/CNT electrocatalysts for oxygen evolution reaction with low overpotential, *RSC Adv.* 6 (2016) 74536–74544, <https://doi.org/10.1039/C6RA16450A>.

[35] C.C.L. McCrory, S. Jung, I.M. Ferrer, S.M. Chatman, J.C. Peters, T.F. Jaramillo, Benchmarking hydrogen evolving reaction and oxygen evolving reaction electrocatalysts for solar water splitting devices, *J. Am. Chem. Soc.* 137 (2015) 4347–4357, <https://doi.org/10.1021/ja510442p>.

[36] C.C.L. McCrory, S. Jung, J.C. Peters, T.F. Jaramillo, Benchmarking heterogeneous electrocatalysts for the oxygen evolution reaction, *J. Am. Chem. Soc.* 135 (2013) 16977–16987, <https://doi.org/10.1021/ja407115p>.

[37] R. Nandan, A. Gautam, K.K. Nanda, Anthocephalus cadamba shaped FeNi encapsulated carbon nanostructures for metal-air batteries as a resilient bifunctional oxygen electrocatalyst, *J. Mater. Chem. A* 6 (2018) 20411–20420, <https://doi.org/10.1039/C8TA05822A>.

[38] T. Fukushima, S. Horike, Y. Inubushi, K. Nakagawa, Y. Kubota, M. Takata, S. Kitagawa, Solid solutions of soft porous coordination polymers: fine-tuning of gas adsorption properties, *Angew. Chem. Int. Ed.* 49 (2010) 4820–4824, <https://doi.org/10.1002/anie.201000989>.

[39] B. Lei, W. Cailing, L. Mei, J. Lifang, W. Guoping, Improving the properties of nickel organic framework as electrode materials for supercapacitors by introducing functional groups, *Int. J. Electrochem. Sci.* 15 (2020) 5758–5769, <https://doi.org/10.20964/2020.06.55>.

[40] Z. Li, X. Wu, X. Jiang, B. Shen, Z. Teng, D. Sun, G. Fu, Y. Tang, Surface carbon layer controllable Ni₃Fe particles confined in hierarchical N-doped carbon framework boosting oxygen evolution reaction, *Adv. Powder Mater.* 1 (2022), 100020, <https://doi.org/10.1016/j.apmate.2021.11.007>.

[41] D. Chen, Q. Sun, C. Han, Y. Guo, Q. Huang, W.A. Goddard, J. Qian, Enhanced oxygen evolution catalyzed by in situ formed Fe-doped Ni oxyhydroxides in carbon nanotubes, *J. Mater. Chem. A* 10 (2022) 16007–16015, <https://doi.org/10.1039/D2TA04042E>.

[42] L. Zhang, J.-S. Hu, X.-H. Huang, J. Song, S.-Y. Lu, Particle-in-box nanostructured materials created via spatially confined pyrolysis as high performance bifunctional catalysts for electrochemical overall water splitting, *Nano Energy* 48 (2018) 489–499, <https://doi.org/10.1016/j.nanoen.2018.04.003>.

[43] D. Xiang, X. Bo, X. Gao, C. Zhang, C. Du, F. Zheng, Z. Zhuang, P. Li, L. Zhu, W. Chen, Novel one-step synthesis of core@shell iron-nickel alloy nanoparticles coated by carbon layers for efficient oxygen evolution reaction electrocatalysis, *J. Power Sources* 438 (2019), 226988, <https://doi.org/10.1016/j.jpowsour.2019.226988>.

[44] S.-W. Park, I. Kim, S.-I. Oh, J.-C. Kim, D.-W. Kim, Carbon-encapsulated NiFe nanoparticles as a bifunctional electrocatalyst for high-efficiency overall water splitting, *J. Catal.* 366 (2018) 266–274, <https://doi.org/10.1016/j.jcat.2018.08.016>.

[45] D. Chen, J. Zhu, X. Mu, R. Cheng, W. Li, S. Liu, Z. Pu, C. Lin, S. Mu, Nitrogen-Doped carbon coupled FeNi₃ intermetallic compound as advanced bifunctional electrocatalyst for OER, ORR and Zn-air batteries, *Appl. Catal., B* 268 (2020), 118729, <https://doi.org/10.1016/j.apcatb.2020.118729>.

[46] Y. Lv, A. Batool, Y. Wei, Q. Xin, R. Bodduula, S.U. Jan, M.Z. Akram, L. Tian, B. Guo, J.R. Gong, Homogeneously distributed NiFe alloy nanoparticles on 3D carbon fiber network as a bifunctional electrocatalyst for overall water splitting, *ChemElectroChem* 6 (2019) 2497–2502, <https://doi.org/10.1002/celc.201900185>.

[47] M. Chen, S. Lu, X.-Z. Fu, J.-L. Luo, Core-shell structured NiFeSn@NiFe (Oxy) hydroxide nanospheres from an electrochemical strategy for electrocatalytic oxygen evolution reaction, *Adv. Sci.* 7 (2020) 1903777, <https://doi.org/10.1002/advs.201903777>.

[48] X. Zhang, Y. Chen, B. Wang, M. Chen, B. Yu, X. Wang, W. Zhang, D. Yang, FeNi nanoparticles embedded porous nitrogen-doped nanocarbon as efficient electrocatalyst for oxygen evolution reaction, *Electrochim. Acta* 321 (2019), 134720, <https://doi.org/10.1016/j.electacta.2019.134720>.

[49] H.-P. Guo, B.-Y. Ruan, W.-B. Luo, J. Deng, J.-Z. Wang, H.-K. Liu, S.-X. Dou, Ultrathin and Edge-Enriched Holey Nitride Nanosheets as Bifunctional Electrocatalysts for the Oxygen and Hydrogen Evolution Reactions, *ACS Catal.* 8 (2018) 9686–9696, <https://doi.org/10.1021/acscatal.8b01821>.

[50] Y. Zhang, X. Hou, X. Li, D. Li, F. Huang, Q. Wei, FeNi alloy nanoparticles embedded in electrospun nitrogen-doped carbon fibers for efficient oxygen evolution reaction, *J. Colloid Interface Sci.* 578 (2020) 805–813, <https://doi.org/10.1016/j.jcis.2020.06.044>.

[51] X. Zhang, H. Xu, X. Li, Y. Li, T. Yang, Y. Liang, Facile synthesis of nickel-iron/nanocarbon hybrids as advanced electrocatalysts for efficient water splitting, *ACS Catal.* 6 (2016) 580–588, <https://doi.org/10.1021/acscatal.5b02291>.

[52] G.-L. Li, X.-C. Xu, B.-B. Yang, S. Cao, X. Wang, X. Fu, Y. Shi, Y. Yan, X. Song, C. Hao, Micelle-template synthesis of a 3D porous FeNi alloy and nitrogen-codoped carbon material as a bifunctional oxygen electrocatalyst, *Electrochim. Acta* 331 (2020), 135375, <https://doi.org/10.1016/j.electacta.2019.135375>.

[53] K. Khan, X. Yan, Q. Yu, S.-H. Bae, J.J. White, J. Liu, T. Liu, C. Sun, J. Kim, H.-M. Cheng, Y. Wang, B. Liu, K. Amine, X. Pan, Z. Luo, Stone-Wales defect-rich carbon-supported dual-metal single atom sites for Zn-air batteries, *Nano Energy* 90 (2021), 106488, <https://doi.org/10.1016/j.nanoen.2021.106488>.

[54] Q. Hu, X. Liu, C. Tang, L. Fan, X. Chai, Q. Zhang, J. Liu, C. He, Facile fabrication of a 3D network composed of N-doped carbon-coated core-shell metal oxides/phosphides for highly efficient water splitting, *Sustain. Energy Fuels* 2 (2018) 1085–1092, <https://doi.org/10.1039/C7SE00576H>.

[55] C. Xie, Y. Wang, K. Hu, L. Tao, X. Huang, J. Huo, S. Wang, In situ confined synthesis of molybdenum oxide decorated nickel-iron alloy nanosheets from Mo₆⁴⁺ intercalated layered double hydroxides for the oxygen evolution reaction, *J. Mater. Chem. A* 5 (2017) 87–91, <https://doi.org/10.1039/C6TA08149E>.

[56] M. Lao, G. Zhao, P. Li, T. Ma, Y. Jiang, H. Pan, S.X. Dou, W. Sun, Manipulating the coordination chemistry of Ru-N(O)-C moieties for fast alkaline hydrogen evolution kinetics, *Adv. Funct. Mater.* 31 (2021) 2100698, <https://doi.org/10.1002/adfm.202100698>.

[57] Y. Shang, Y. Ding, P. Zhang, M. Wang, Y. Jia, Y. Xu, Y. Li, K. Fan, L. Sun, Pyrrolic N or pyridinic N: the active center of N-doped carbon for CO₂ reduction, *Chin. J. Catal.* 43 (2022) 2405–2413, [https://doi.org/10.1016/S1872-2067\(22\)64122-6](https://doi.org/10.1016/S1872-2067(22)64122-6).

[58] T. Wu, S. Sun, J. Song, S. Xi, Y. Du, B. Chen, W.A. Sasanka, H. Liao, C.L. Gan, G. Scherer, L. Zeng, H. Wang, H. Li, A. Grimaud, Z.J. Xu, Iron-facilitated dynamic active-site generation on spinel CoAl₂O₄ with self-termination of surface reconstruction for water oxidation, *Nat. Catal.* 2 (2019) 763–772, <https://doi.org/10.1038/s41929-019-0325-4>.

[59] X. Yang, L. Kang, Z. Wei, S. Lou, F. Lei, P. Hao, J. Xie, B. Tang, A self-sacrificial templated route to fabricate CuFe Prussian blue analogue/Cu(OH)₂ nanoarray as an efficient pre-catalyst for ultrastable bifunctional electro-oxidation, *Chem. Eng. J.* 422 (2021), 130139, <https://doi.org/10.1016/j.cej.2021.130139>.

[60] J. Zhang, R.-Z. Sun, X.-F. Zhang, J.-X. Wu, Y.-H. Dou, X.-Y. Zhu, L.-H. Yu, L.-Y. Guo, M.-L. Liu, L. Guo, L.-M. Cao, C.-T. He, X.-M. Chen, Biodiversity benefits for size modulation of metal nanoparticles to achieve in situ semi-oxidation toward optimized electrocatalytic oxygen evolution, *Adv. Funct. Mater.* 32 (2022) 2202119, <https://doi.org/10.1002/adfm.202202119>.

[61] J. He, X. Zhou, P. Xu, J. Sun, Promoting electrocatalytic water oxidation through tungsten-modulated oxygen vacancies on hierarchical FeNi-layered double hydroxide, *Nano Energy* 80 (2021), 105540, <https://doi.org/10.1016/j.nanoen.2020.105540>.

[62] H. Qiao, Y. Yang, X. Dai, H. Zhao, J. Yong, L. Yu, X. Luan, M. Cui, X. Zhang, X. Huang, Amorphous (Fe)Ni-MOF-derived hollow (bi)metal/oxide@N-graphene polyhedron as effectively bifunctional catalysts in overall alkaline water splitting, *Electrochim. Acta* 318 (2019) 430–439, <https://doi.org/10.1016/j.electacta.2019.06.084>.

[63] H. Krohn, Transport of intercalated anions in graphite—an electrochemical investigation, *Carbon* 23 (1985) 449–457, [https://doi.org/10.1016/0008-6223\(85\)90040-5](https://doi.org/10.1016/0008-6223(85)90040-5).

[64] I.J. Suárez, T.F. Otero, M. Márquez, Diffusion coefficients in swelling polypyrrrole: ESCR and cottrell models, *J. Phys. Chem. B* 109 (2005) 1723–1729, <https://doi.org/10.1021/jp046051q>.

[65] D. Pletcher, A. First Course in Electrode Processes, The Royal Society of Chemistry 2009.

[66] C. Liang, P. Zou, A. Nairan, Y. Zhang, J. Liu, K. Liu, S. Hu, F. Kang, H.J. Fan, C. Yang, Exceptional performance of hierarchical Ni-Fe oxyhydroxide@NiFe alloy nanowire array electrocatalysts for large current density water splitting, *Energy Environ. Sci.* 13 (2020) 86–95, <https://doi.org/10.1039/C9EE02388G>.

[67] X. Shan, J. Liu, H. Mu, Y. Xiao, B. Mei, W. Liu, G. Lin, Z. Jiang, L. Wen, L. Jiang, An engineered superhydrophilic/superaerophobic electrocatalyst composed of the supported CoMoS_x chalcogel for overall water splitting, *Angew. Chem. Int. Ed.* 59 (2020) 1659–1665, <https://doi.org/10.1002/anie.201911617>.